Published in final edited form as:

Nature. 2017 October 19; 550(7676): 411–414. doi:10.1038/nature24055.

Cryo-EM structure of the lysosomal Ca^{2+}-permeable channel TRPML3

Marscha Hirschi[1,†], **Mark A. Herzik Jr.**[2,†], **Jinhong Wie**[3], **Yang Suo**[1], **William F. Borschel**[1], **Dejian Ren**[3], **Gabriel C. Lander**[2,*], and **Seok-Yong Lee**[1,*]

[1]Department of Biochemistry, Duke University School of Medicine, Durham, North Carolina, 27710, USA

[2]Department of Integrative Structural and Computational Biology, The Scripps Research Institute, La Jolla, California, 92037, USA

[3]Department of Biology, University of Pennsylvania, Philadelphia, Pennsylvania 19104, USA

Summary

The modulation of ion channel activity by lipids is increasingly recognized as a fundamental component of cellular signaling. The mucolipin transient receptor potential (TRPML) channel family belongs to the TRP superfamily[1,2] and is composed of three members, TRPML1-3. TRPMLs are the major Ca^{2+}-permeable channels on late endosomes and lysosomes (LEL). They regulate organelle Ca^{2+} releases important for various physiological processes, including organelle trafficking and fusion[3]. Loss-of-function mutations in the TRPML1 gene cause the neurodegenerative lysosomal storage disorder mucolipidosis IV (ML-IV), and a gain-of-function mutation in TRPML3 (Ala419Pro) gives rise to the Varitint-Waddler (*Va*) mouse phenotype[4–6]. Notably, TRPMLs are activated by the low-abundance and LEL-enriched signaling lipid $PI(3,5)P_2$, while other phosphoinositides such as $PI(4,5)P_2$, enriched in plasma membranes, inhibit TRPMLs[7,8]. Conserved basic residues at the N-terminus of the channels are important for $PI(3,5)P_2$ activation and $PI(4,5)P_2$ inhibition[8]. However, due to a lack of structural information, the mechanism by which TRPML channels recognize $PI(3,5)P_2$ and increase its Ca^{2+} conductance remains elusive. Here we present the cryo-electron microscopy (cryo-EM) structure of a full-length TRPML3, at an average resolution of 2.9 Å. Our structure reveals not only the molecular basis of ion conduction but also the unique architecture of TRPMLs, wherein the voltage sensor-like domain is linked to the pore via a cytosolic domain we term the “mucolipin domain” (MLD). Combined with functional studies, we suggest that the MLD is responsible for $PI(3,5)P_2$ binding

*Correspondence to: S.-Y. Lee, seok-yong.lee@duke.edu, telephone: 919-684-1005; G.C. Lander, glander@scripps.edu, telephone: 858-784-8793.

†These authors contributed equally.

Competing financial interests The authors declare no competing financial interests.

Author Contributions M.H. conducted biochemical optimization of TRPML3 for structure determination and model building under the guidance of S.-Y.L. M.A.H. conducted all electron microscopy experiments and the single-particle 3D reconstruction under the guidance of G.C.L. J.W. performed all the lysosome electrophysiology recordings under the guidance of D.R. Y.S. and W.F.B. carried out $PI(3,5)P_2$ binding and whole-cell patch recordings, respectively under the guidance of S.-Y.L. S.-Y.L., G.C.L., D.R., M.H. and M.A.H. wrote the paper.

and subsequent channel activation, and that it acts as a 'gating pulley' for lipid-dependent TRPML gating.

These studies utilized TRPML3 from the common marmoset, *Callitrix jacchus*, ($TRPML3_{wt}$, 97% sequence identity to human TRPML3) (Extended Data Fig. 1) harboring a putative glycosylation knockout mutation (Asn138Gln, $TRPML3_{NQ}$). Whole-cell electrophysiological recording shows that $TRPML3_{wt}$ is fully functional and that the Asn138Gln mutation does not appreciably affect channel function (Extended Data Fig. 2)[6,9–11]. Single particle cryo-EM analyses produced a 3D reconstruction of $TRPML3_{NQ}$ at an overall resolution of ~2.9 Å (See Methods and Extended Data Fig. 3), which allowed for *de novo* model building (Fig. 1, Extended Data Figs. 3 and 4, and Extended Data Table 1). Several non-protein densities were resolved in the cryo-EM map, which we assigned as lipid molecules (Fig. 1a, Extended Data Fig. 5). Lipid molecules were observed at analogous sites in both PKD2 and TRPV1 structures[12–14].

TRPML3 can be divided into three domains: the extracytosolic domain (ECD), the transmembrane channel (TM) domain, and the cytosolic domain (Fig. 1). The ECD is composed of two beta sheets and two extracytosolic helices, which tetramerize into a ring that caps the extracytosolic side of the channel (Fig. 1d), and is structurally similar to the ECDs of TRPML1[15] and PKD2[12,13,16] (Extended Data Fig. 6). Unlike PKD2, the interactions between the ECD and the TM domain are minimal, being mostly limited to the voltage sensor-like domain (VSLD)[12,13,16] (Extended Data Fig. 6). Three histidines within the ECD have been shown by mutagenesis to play an important role in TRPML3 pH sensing[9]. The location of these critical residues at ECD-ECD and ECD-TM interfaces suggest that pH sensing may involve histidine-mediated structural rearrangements (Fig. 1d).

The architecture of the TRPML3 TM domain resembles the bacterial voltage-gated Na^+ channel, comprising a domain-swapped homotetramer with a VSLD made up of S1-S4 and a pore formed by S5, S6, and two pore helices (P1 and P2) (Fig. 1e). The TM domain has three prominent features. First, TRPML3 does not contain a "TRP domain", a hallmark of most TRP channels[17–20]. Second, S4 in TRPML3 is entirely alpha helical, in marked contrast with other TRP channels that contain a 3_{10}-helix (Extended Data Fig. 6)[13,17–19,21]. The 3_{10}-helix appears to confer mobility for vanilloid-dependent conformational changes in TRPV1[18]. Third, multiple TMs protrude out of the membrane, with S1 extending ~18 Å into the lysosomal lumen, and S2 extending ~24 Å into the cytosol (IS2) (Fig. 1a, b). The S1 extension establishes a larger interaction interface with the pore than seen in TRPV1, TRPV2, and PKD2 (Extended Data Fig. 6)[13,18,19].

A defining feature of TRPMLs is the cytosolic domain (Fig. 1f). IS2 interacts with short intracellular helices connected to S1 and S3 (IS1a, IS1b, and IS3). Notably, a short helix (IS6), connected to S6, interacts with IS1, IS2, and IS3, forming an intracellular helical bundle that we refer to as the "mucolipin domain" (MLD) (Fig. 1).

The tetrameric ECD ring forms a vestibule above the transmembrane domain with central and lateral openings that are both too large to function as barriers for ion flow (Extended Data Fig. 6). The selectivity filter is located between the two pore helices, formed by the

backbone carbonyls of Asn456 and Gly457 and the sidechains of Asp458 and Asp459 (Fig. 2 and Extended Data Fig. 7). Notably, we observed three cryo-EM density peaks (2.9–9.9 sigma) within the selectivity filter that we term Sites 1 to 3. Due to the ion composition in the sample (150 mM Na^+), we tentatively assigned these peaks as sodium ions (Fig. 2). The minimum radius of the selectivity filter is 2.2 Å, which is wide enough to accommodate partly hydrated Ca^{2+} or Na^+. The hydrated Site 1 ion is coordinated by the carboxylate groups of Asp458 and Asp459, Site 2 mainly by the backbone carbonyls of Gly457, and Site 3 mainly by the backbone carbonyl groups of Asn456. There are three additional putative ion peaks in the cavity below the selectivity filter, which we term Sites 4 to 6.

The C-terminal portions of the four S6 helices come into close proximity and form a constriction we term “the S6 gate” (Fig. 2). The minimum radius of the S6 gate at the side chains of Ile498 is ~1 Å, allowing only the passage of dehydrated ions. This conformation may represent a closed state, although a resting state that allows for a low basal current at negative potential cannot be ruled out (Extended Data Fig. 2). A pi helix, a rare helix with a wider turn (4.1 residues per turn) than an alpha helix (3.6 residues per turn), is observed in the middle of S6, introducing a kink that redirects the C-terminal end of the helix towards the pore to form the S6 gate. Several TRP channels contain a pi helix in S6[13,17,22], a structural feature previously proposed to function as a hinge that endows S6 with a gating capacity[19].

TRPML3 is highly selective for Ca^{2+} over K^+, and appears to be more selective for Ca^{2+} over Na^+, but the molecular basis for ion selectivity is not well understood[9]. Unlike Ca^{2+} or Na^+, K^+ would only fit in the selectivity filter in its dehydrated form and cannot optimally interact with the selectivity filter, likely contributing to the high selectivity of TRPML3 for Ca^{2+} over K^+. Notably, the configuration of the selectivity filter, composed of the two backbone carbonyls and two aspartate residues, is reminiscent of the engineered Ca^{2+}-selective voltage-gated ion channel Ca_VAb[23]. High-resolution structures of Ca_VAb and the bacterial sodium channel Na_VM reveal selectivity filters containing three ion-binding sites similar to TRPML3[23,24] (Fig. 2). In both Ca_VAb and Na_VM, electrostatic energetics of Site 1 was suggested to be important for conferring respective ion selectivity[23,24]. Consistent with this idea, mutating Asp459 to alanine rendered TRPML3 less selective and permeant for calcium[25]. In the TRPML3 reconstruction, the Na^+ density peak at Site 1 is appreciably weaker than those at Sites 2 and 3. Because Site 2 and Site 3 are unlikely to be occupied at the same time due to their proximity (2.8 Å), approximately one Na^+ ion can occupy the selectivity filter (either at Site 2 or at Site 3), while two Ca^{2+} ions could occupy the selectivity filter simultaneously (at Sites 1 and 2 or at Sites 1 and 3), further contributing to the Ca^{2+} selectivity of TRPML3. We also suggest that Sites 4 and 5 are occupied in an alternating fashion along with Site 2 and Site 3, respectively. The major populated states for Na^+ ions in the selectivity filter are summarized in Fig. 2c.

In contrast to TRPV1 and TRPV2, the TRPML3 selectivity filter is part of an extensive structural network that resembles the selectivity filters of Ca_VAb and Na_VM, which do not act as gates. Therefore, we propose that the S6 gate is solely responsible for TRPML3 channel gating.

Using isothermal titration calorimetry (ITC), we found that dioctanoyl (diC_8)-PI(3,5)P_2, binds to $TRPML3_{NQ}$ with a K_d of ~2.5 μM (Fig. 3d). There is a large pocket between the VSLD and the MLD, formed by IS1a, IS1b, and IS2, with an entrance lined by basic amino acids (Fig. 3). Distinct sets of these residues in IS1a and IS1b have been implicated in PI(3,5)P_2 and PI(4,5)P_2 binding by TRPML1[7,8]. PI(3,5)P_2 occupies this pocket in our docking studies with the headgroup positioned at the pocket entrance (Extended Data Fig. 5e–f). Point mutations in the putative PI(3,5)P_2 binding site (Arg58Ala, Lys62Ala, Tyr342Ala, and Arg305Ala) result in a substantial reduction in diC_8-PI(3,5)P_2 binding and a triple mutation (Lys52Ala/Arg58Ala/Lys62Ala) shows no measureable binding by ITC (Fig. 3d, Extended Data Fig. 2, Extended Data Table 2).

Furthermore, electrophysiological recordings from lysosomes showed that the Arg58Ala point mutation substantially reduced PI(3,5)P_2-activated TRPML3 current and the triple mutant (Lys52Ala/Arg58Ala/Arg62Ala) showed no PI(3,5)P_2-mediated activation (Figs. 3e, f and Extended Data Fig. 2). Remarkably, a point mutation of Arg305 (Arg305Ala), a residue located on S2 that has not been previously implicated in PI(3,5)P_2 binding[7,8], abolished PI(3,5)P_2-mediated activation (Fig. 3e, f). To test if the effect of the Arg305Ala mutation is due to altered expression or targeting, we introduced the gain-of-function mutation Ala419Pro[10] to the Arg305Ala mutant. The Ala419Pro mutation likely locks S6 in an open conformation due to the position of Ala419 near the pi helix on S6 (Extended Data Fig. 8). The Arg305Ala/Ala419Pro mutant generated substantial inwardly-rectifying currents in the presence or absence of PI(3,5)P_2 (Fig. 3e, f), suggesting that the Arg305Ala is properly expressed and the Ala419Pro mutation bypasses PI(3,5)P_2-dependent activation. Taken together, our data show that the pocket of the MLD serves as a PI(3,5)P_2 binding site, and that interaction of PI(3,5)P_2 with Arg305 in S2 may be key to TRPML3 activation.

IS1a, IS2, and IS3, which form the core of the MLD, create a docking site for three conserved hydrophobic residues from IS6 (Leu521, Phe524, Ile525) (Fig. 3c). The novel architecture of the MLD and its linkage to S6 via IS6 appears to enable direct communication of PIP_2 binding to the S6 gate. Mutation of Phe524 to alanine substantially reduced PI(3,5)P_2-mediated TRPML3 currents in lysosomal electrophysiological recordings (Fig. 3e, f). Introduction of Ala419Pro into the Phe524Ala mutant restored the channel current, confirming proper channel assembly and trafficking (Fig. 3e, f).

Together, our findings reveal the structural basis for ion conduction by TRPML3, and suggest a model by which TRPML gating may be controlled through discriminative binding of different PIP_2 species. We speculate that PI(3,5)P_2 binding induces a conformational change in S2, which pulls on S6 via the MLD to open the S6 gate. In contrast, PI(4,5)P_2 binding likely causes a differential S2 movement leading to a gate closure (Fig. 3g). We propose that S2 is the primary mobile unit associated with phosphoinositide binding and that the MLD acts as a “gating pulley”, based on our findings that (i) Arg305 in S2 appears important for PI(3,5)P_2 binding and activation, (ii) S2 is connected to the MLD as a continuous helix (IS2), (iii) the facts that S1 interacts extensively with the pore and S4 is entirely alpha-helical make these two helices unlikely candidates as a mobile unit, and (iv) interaction of Phe524 in IS6 with the MLD appears important for PI(3,5)P_2-dependent activation. Our proposed gating pulley model is based on several assumptions and further

study of PIP_2-bound TRPML structures will be required to test this model. Finally, given the high sequence conservation, the PIP_2-dependent gating mechanism is likely conserved between TRPML1 and TRPML3 (Extended Data Fig. 1), with our structure providing the framework to elucidate the molecular basis of mutations that cause ML-IV (Extended Data Fig. 8)[26–29].

Methods

No statistical methods were used to predetermine sample size. The experiments were not randomized, and investigators were not blinded to allocation during experiments and outcome assessment.

Protein expression and purification

In order to identify a stable TRPML3 ortholog for structure determination a total of 31 orthologs were subjected to an expression screen. Genes were codon-optimized for expression in *Spodoptera frugiperda* (Sf9) cells. Mutant constructs were prepared using the Quikchange mutagenesis kit (Agilent). For expression, constructs were cloned into a pFastBac vector with a C-terminal FLAG- and His-tag, cleavable by PreScission Protease (PPX). Constructs were transformed into DH10Bac cells for bacmid preparation, which were isolated from 2 mL overnight cultures by isopropanol precipitation. Virus was prepared according to manufacturer's manual (Invitrogen, Bac-to-Bac). Protein was expressed in Sf9 cells at a cell density of 1.5 M mL^{-1} and grown at 27 °C for 60–65 h. Cells were harvested by centrifugation at 1710 × g and resuspended in lysis buffer (50 mM Tris pH 8, 150 mM NaCl, 2 mg mL^{-1} iodoacetamide, 1.4 mM β-mercaptoethanol, 1 μg mL^{-1} leupeptin, 1 μg mL^{-1} pepstatin, 0.66 μg mL^{-1} aprotinin and 1mM phenylmethylsulfonyl fluoride). Cells were lysed by homogenization or sonication (3 × 30 pulses) and protein was extracted in 40 mM dodecyl maltopyranoside (DDM) and 4 mM cholesteryl hemisuccinate (CHS) Tris salt (Anatrace) for 1 hr at 4 °C under gentle agitation. The insoluble fraction was removed by centrifugation. Anti-FLAG M2 resin (Sigma-Aldrich) was applied to the lysate and protein binding performed for 1 h at 4 °C under gentle agitation. The resin was packed onto a column and washed with 5 column volumes of DDM buffer (20 mM Tris pH 8, 150 mM NaCl, 1 mM DDM, 0.1 mM CHS and 2 mM DTT) and 10 column volumes of DM wash buffer (20 mM Tris pH 8, 150 mM NaCl, 4 mM decyl maltopyranoside (DM), 0.1 mM CHS and 2 mM DTT). Protein was eluted with 5 column volumes of DDM buffer supplemented with 100 μg mL^{-1} FLAG peptide. The protein was concentrated to 1 mg mL^{-1} and the tag was cut overnight with PPX at 4 °C. Protein was exchanged into DM buffer by concentration and 10 times dilution in DM buffer. Subsequently, the protein was applied to a Superose-6 size exclusion column in DM buffer. Peak fractions were concentrated and PMAL-8 was added at 1:3 mass ratio of TRPML3:PMAL-8 and incubated overnight. Biobeads were added (15 mg mL^{-1}) and incubated for 4 h at 4 °C. A final size exclusion chromatography step was performed in HEPES pH 7.4, 75 mM NaCl and 75 mM KCl to remove excess amphipols.

EM sample preparation

For negatively-stained TRPML3, 4 μL of amphipol-solubilized protein (0.04 mg/mL) was applied to a freshly glow-discharged 400 Cu-Rh Maxtaform grid (Electron Microscopy Services) that had been coated with a thin layer of carbon. After incubation on grid for ~90s, excess solution was wicked away using Whatman #1 filter paper and 5 μL of ~1% (w/v) uranyl formate solution was immediately applied directly to the grid. After ~10s, excess stain was wicked away and the grid surface was 3x repeated washed with 25 μL 1% (w/v) UF solution to yield thorough embedding of the sample. Following the final wash the grid was blotted to dryness and allowed to air-dry in a fume hood.

For cryo-EM, 3 uL of purified amphipol-solubilized TRPML3 (0.5 mg/ml) was applied to a freshly plasma cleaned (75% argon/25% oxygen atmosphere, 15 Watts for 6 seconds in a Gatan Solarus) UltrAuFoil® R1.2/1.3 300-mesh grid (Electron Microscopy Services) and manually blotted using filter paper (Whatman No.1) for ~4 seconds (≥95% relative humidity, 4°C) immediately prior to plunge freezing in liquid ethane cooled by liquid nitrogen.

EM image acquisition and data processing

All EM data were acquired using the Leginon automated data acquisition program[30] and all image pre-processing was performed concurrently with data collection using the Appion image-processing pipeline[31]. Images of negatively-stained TRPML3 were acquired on a Tecnai Spirit (FEI) transmission electron microscope (TEM) operating at 120 keV. Images were collected at a nominal magnification of 52000× on a Tietz TVIPS F416 camera, corresponding to a pixel size of 2.05 Å/pixel at specimen level. All micrographs were collected with an electron dose of ~25 electrons/Å^2 with a defocus range of −0.8 to −1.6 μm. 265 images were used for automated particle picking using Difference of Gaussians (DoG) picker[32] to yield 17,080 particles. CTF estimation was performed using CTFFind4[33] and whole-image phase-flipping was performed using EMAN[34] prior to particle extraction. 17,080 2x binned particles were extracted and subjected to reference-free 2D classification using multivariate statistical analysis (MSA) and multi-reference alignment (MRA)[35] in the Appion pipeline. Classes representing intact particles were isolated and a resulting stack of 8,928 particles were subjected to 3D classification (k=3, tau fudge=2) using RELION v1.4[36] with a 60 Å low-pass filtered map of EMD-5778 as an initial model. The best class representing 3,457 particles was then refined (C4 symmetry imposed) using the final outputted map from 3D classification as an initial model.

Images of frozen-hydrated TRPML3 were collected on a Titan Krios (FEI) operating at 300 keV equipped with a K2 Summit direct electron detector operating in super-resolution mode. 2,259 movies were collected at a nominal magnification of 22500× with a physical pixel size of 1.31 Å/pixel (0.655 Å/pixel super-resolution pixel size) using a defocus range of −0.8 to −2.8 μm. Each movie (48 frames) was acquired using a dose rate of ~9 electrons/pixel/second over 12 seconds yielding a cumulative dose of ~63 electrons/Å^2. The MotionCor frame alignment program[37] was used to motion-correct the Fourier-binned 2 × 2 (1.31 Å/pix) super-resolution frames using a 3 frame running average window. Aligned images were used for CTF determination using CTFFIND4[33] and only micrographs yielding CC estimates better than 0.5 at 4 Å resolution were kept. DoG picker[32] was used to

automatically pick particles from the first 50 micrographs yielding a stack of 20,571 particles binned by 4 (5.24 Å/pixel, 64 pixel box size) which were then subjected to reference-free 2D classification using MSA/MRA[35] in the Appion pipeline. The best 8 classes were then used as template for particle-picking against the entire dataset using FindEM[38]. A final particle 4x binned stack of 839,127 particles were extracted (5.24 Å/pixel, 64 pixel box size) using RELION v1.4[36] and subjected to reference-free 2D classification. Classes that exhibited high-resolution features were then selected (498,612 particles) for a 3D refinement into a single class using the negative stain reconstruction as an initial model. Following refinement, particles were re-centered and re-extracted without binning (1.31 Å/pixel, 256 pixel box size) and subjected to 3D auto-refinement with C4 symmetry imposed. The refinement was continued using a soft-mask (3 pixel extension, 5 pixel soft cosine edge) generated from a volume contoured to display the full density[39]. These particles were then subjected to 3D classification (k=4, tau fudge=8) without angular or translational searches using a soft mask contoured to show only the protein density. The highest resolution class (104,084 particles) was then further refined using the same soft protein-only mask to yield a 3.53 Å resolution reconstruction as determined by gold-standard 0.143 Fourier shell correlation (FSC)[40,41]. Subsequent movie-refinement (with a running average of 7 frames) was followed by particle polishing (using a standard deviation of 300 pixels on the inter-particle distance and a 3 frame B-factor running average) with a soft mask generated against the full molecule. These “shiny” particles were then refined using a soft protein-only mask to yield a final reconstruction determined to 3.02 Å resolution (gold-standard FSC). Super-resolution movies were then aligned using MotionCor2 on 5 × 5 tiled frames with a B-factor of 100 applied and dose-weighting being performed[42]. The refined particles coordinates from the final highest-resolution class were used to extract 2x binned particles (1.31 Å/pixel, 256 box size) and subjected to 3D auto-refinement using RELION 2.0[43]. Particles were re-centered and re-extracted from unbinned, dose-weighted summed images (0.655 Å/pixel, 512 box size) and subjected to 3D auto-refinement using a soft protein-only mask. The final resolution was estimated to 2.94 Å using phase-randomization to account for the convolution effects of a solvent mask on the FSC between the two independently refined half maps[44]. The ‘blocres’ function in the Bsoft package[45] was used to perform local resolution estimation, based on the two half-volumes outputted from the RELION 3D auto-refinement. All display images were generated using UCSF Chimera[46].

Model building and refinement

The model of TRPML3 was built *de novo* into the electron density map in Coot, using the TRPV2 structure (PDB ID: 5AN8) as a guide for the channel region[47]. Idealized helices and beta strands were placed in the electron density and rigid body refined. Bulky sidechains were built and used to determine the register of helices and beta stands. Subsequently, the loops were built to connect the secondary structural elements. Side chains were built into the electron density adhering to optimal rotamer conformations as indicated by electron density. The structure was real space refined in Coot[47] constrained to ideal geometry and secondary structure where appropriate. Several non-protein densities were observed into which CHS molecules and partial phospholipid molecules were built, based on the shape of the density and buffer composition. Finally, the model was iteratively real-space refined using the

Phenix command line by global minimization and rigid body refinement with a high weight on ideal geometry and restrained to secondary structure[48]. The B factors were set to 30 A^2 for the protein and 50 A^2 for lipid molecules, after which the B factors were refined using the Phenix command line. The model was further manually optimized in Coot for adherence to geometric restraints using Molprobity (http://molprobity.biochem.duke.edu/) to identify problematic regions. After we built our model, the crystal structure of the TRPML1 ECD fragment (PDB ID: 5TJA) was reported which we used to confirm the accuracy of our model. The final model excludes 32 residues at the N-terminus, two short loops in the ECD (residues 148–153 and residues 197–200), and 27 residues at the C-terminus. FSCs of the half maps against the refined model agreed well with each other, showing that our model is not over-refined (Extended Data Fig. 3). Radius along the permeation pathway was calculated using HOLE[49]

Cell culture and transfections

HEK293T cells (62312975 – ATCC) were grown in DMEM supplemented with 10 % FBS (Gibco or Atlanta Biologicals), 1 % penicillin/streptomycin (Gibco) and were sustained in 5 % CO_2 atmosphere at 37 °C. The cell lines used in this study have not been further authenticated. The cells for whole cell electrophysiological recordings were tested for mycoplasma contamination. Cells between passage 5 – 30 grown in 40-mm wells (or 20-mm wells for lysosomal recordings) were transiently transfected at 30 – 50 % confluency. For whole-cell recording, 0.8 μg pEG BacMam plasmid[50] encoding TRPML3 and 0.2 μg pcDNA plasmid encoding GFP were transfected using FuGene6 (Promega). Transfection mixtures of DNA were incubated for 1.5 hours at room temperature and added to each correspond well. Transfected cells were reseeded onto 12-mm round glass coverslips (Fisher) 24 hr post transfected and used 12 – 24 hours after for electrophysiological experiments. For lysosomal recordings, GFP-tagged TRPML3 at its C-terminus (TRPML3-GFP) was subcloned into pEG BacMam plasmid[50]. Each 20-mm well was transfected with 0.5 μg plasmid encoding TRPML3-GFP using PolyJet (SignaGen Laboratories) following the manufacture's protocol.

Lysosomal electrophysiology

Whole-lysosome patch clamp recordings were done as previously described[51]. Briefly, transfected cells were re-plated onto 12-mm coverslips ~36 hr after transfection. Lysosomes were enlarged with vacuolin-1 (1 μM, overnight) and were released from cells using glass pipettes. Polished glass pipettes used for patch-clamp recordings had resistance of 5–8 MΩs. Pipette solution (lumen) contained (in mM) 145 NaCl, 5 KCl, 1 $MgCl_2$, 2 $CaCl_2$, 10 HEPES, 10 MES and 10 glucose (pH adjusted to 4.6 with NaOH). Bath solution contained (in mM) 140 K-gluconate, 4 NaCl, 2 $MgCl_2$, 0.39 $CaCl_2$, 1 EGTA and 10 HEPES (pH adjusted to 7.2 with KOH). Recordings were done 48 - 72 hr after transfection. Signals were amplified and filtered at 1 KHz using a MultiClamp 700B amplifier, and digitized at 5 KHz with a Digidata 1400A digitizer, both controlled with Clampex 10.4 (from Molecular Devices). Lysosomes were held at 0 mV. Current-voltage relationships were obtained using a ramp protocol from −100 mV to +50 mV in 1 s. Data were analyzed using Clampfit 10.4 (Molecular Devices), Excel (Microsoft) and Origin (Origin Lab).

Whole-cell recordings

Whole-cell voltage-clamp experiments were performed with glass electrodes pulled from borosilicate glass capillaries (Sutter Instruments) with a final resistance of 2 – 5 MΩ. The intracellular pipette solution contained (in mM) 150 CsCl, 2 $MgCl_2$, 5 EGTA, 10 HEPES, 4 Mg-ATP, adjusted to pH 7.2 (CsOH), and osmolarity of 280 ± 5 mOsm L^{-1}. Glass coverslips were loaded into an open bath chamber (RC-26G, Warner Instruments) and all extracellular solutions were applied with a gravity driven perfusion system that could completely exchange the bath solutions within 10 – 20 s.

Whole-cell current responses were elicited every 5 s with a continuous repeating voltage ramp protocol (holding potential 0 mV, 400-ms voltage ramp from 100 to −100 mV). Current responses were low-pass filtered at 2 kHz (Axopatch 200B), digitally sampled at 10 kHz (Digidata 1440A), converted to digital files in Clampex10.7 (Molecular Devices) and stored on an external hard drive for offline analyses (Clampfit10.7).

Cells were first bathed in an extracellular solution containing (in mM) 140 NaCl, 5 KCl, 2 $MgCl_2$, 1 CaCl 10 mM HEPES at pH 7.4 (NaOH) and osmolarity of 290 ± 5 mOsm L^{-1} followed by a 0 Na solution containing (in mM) 150 NMDG, 10 HEPES at pH 7.4 (HCl) and osmolarity of 290 ± 5 mOsm L^{-1}. Bath solutions containing either 20 μM or 80 μM 5-mesityl-3-oxa-4-azatricyclo[5.2.1.0~2,6~]dec-4-ene (SN-2; Specs; prepared daily from DMSO stocks (10 mM) stored at −80 °C; final DMSO 0.8 %) were applied until the current at −100 mV no longer increased in amplitude. Leak conductance was assessed at the end of each recording by the residual current at −100 mV after application of the 0 Na solution.

Isothermal titration calorimetry

All mutants were prepared in the $TRPML_{NQ}$ background using Quikchange mutagenesis kit (Agilent). Protein was expressed and purified as described previously, except that CHS was omitted from all buffers and the sample was kept in DDM buffer at all times. After binding, the FLAG resin was loaded onto a gravity column and washed with 10 column volumes of DDM buffer. The sample was eluted in DDM buffer supplemented with 100 μg mL^{-1} FLAG peptide. The tag was cut overnight and protein was further purified by Superose-6 size exclusion in DDM buffer. Protein was concentrated to ~80 μM for ITC experiments performed on a MicroCal ITC200 system. 800 μM $PI(3,5)P_2$ was titrated 1.6 μL at a time into an 80 μM protein solution. The curves were fit to a single-site binding isotherm using the Malvern Instruments software.

Docking of $PI(3,5)P_2$ to TRPML3

Docking of $PI(3,5)P_2$ to $TRPML3_{WT}$ was performed using AutoDock Vina[52]. The initial coordinates of 1-arachidolyl,2-stearyl-*sn*-glycero-3-phospho-(1-D-*myo*-inositol 3,5-bisphosphate) molecule was generated from the SMILES string using PHENIX.eLBOW, and stereochemistry was manually corrected in PHENIX.REEL. In particular, the *myo*-configuration of the inositol ring and double bonds in the lipid tail were examined and corrected if necessary. Before docking, the sidechains of residues K41, K52, R56, R58, K59, K62, R305, and Y342 of $TRPML3_{WT}$ were set as flexible. Docking was carried out over a search space of 70 × 56 × 110 Å that covers the entire putative PIP_2 binding cavity formed

by IS1, IS2, IS3 and IS6. Seven out of the nine output poses exhibited similar conformations, where the 3′- and 5′-phosphates of $PI(3,5)P_2$ interact with the positively charged residues in the pocket, especially R52, R58, and K62. One representative docking result was shown in Extended Data Fig. 6. Docking results were visualized and analyzed with PyMol.

Data availability statement

The sequence of $TRPML3_{CJ}$ can be found in the National Center for Biotechnology Information under accession code JAB18777.1. The coordinates are deposited in the Protein Data Bank with the PDB ID 5W3S and the electron density maps have been deposited in EMDB with the ID EMD-8764.

Extended Data

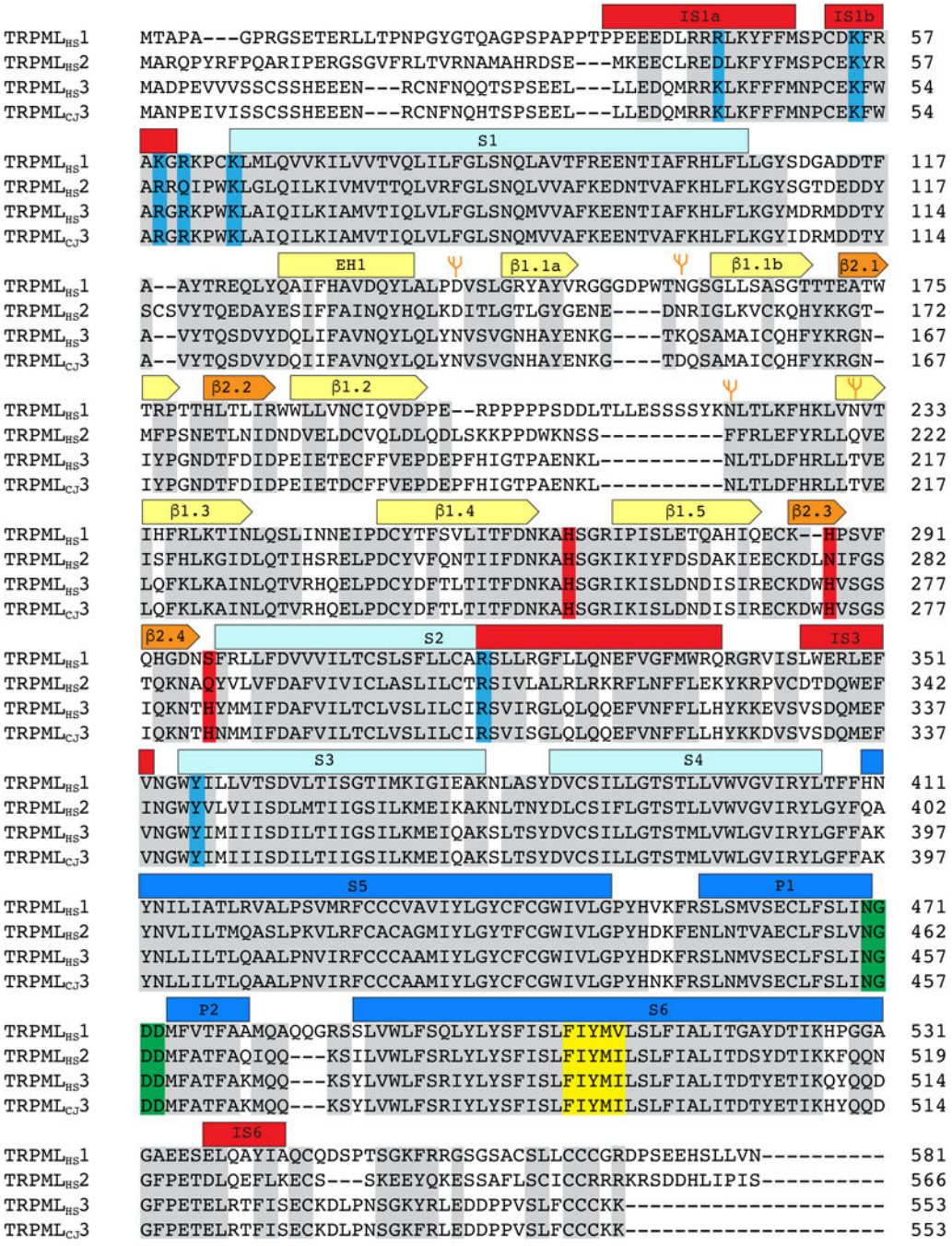

Extended Data Figure 1. Sequence alignment of TRPMLs

Secondary structure elements are indicated by rectangles (helices) and arrows (beta strands). Colored as in Fig. 1. Residues with sequence conservation are highlighted in grey, the selectivity filter in green, the pi helix in yellow, the pH-sensing histidines in red, and putative PIP_2 binding residues in blue. Potential glycosylation sites are indicated by an orange branch.

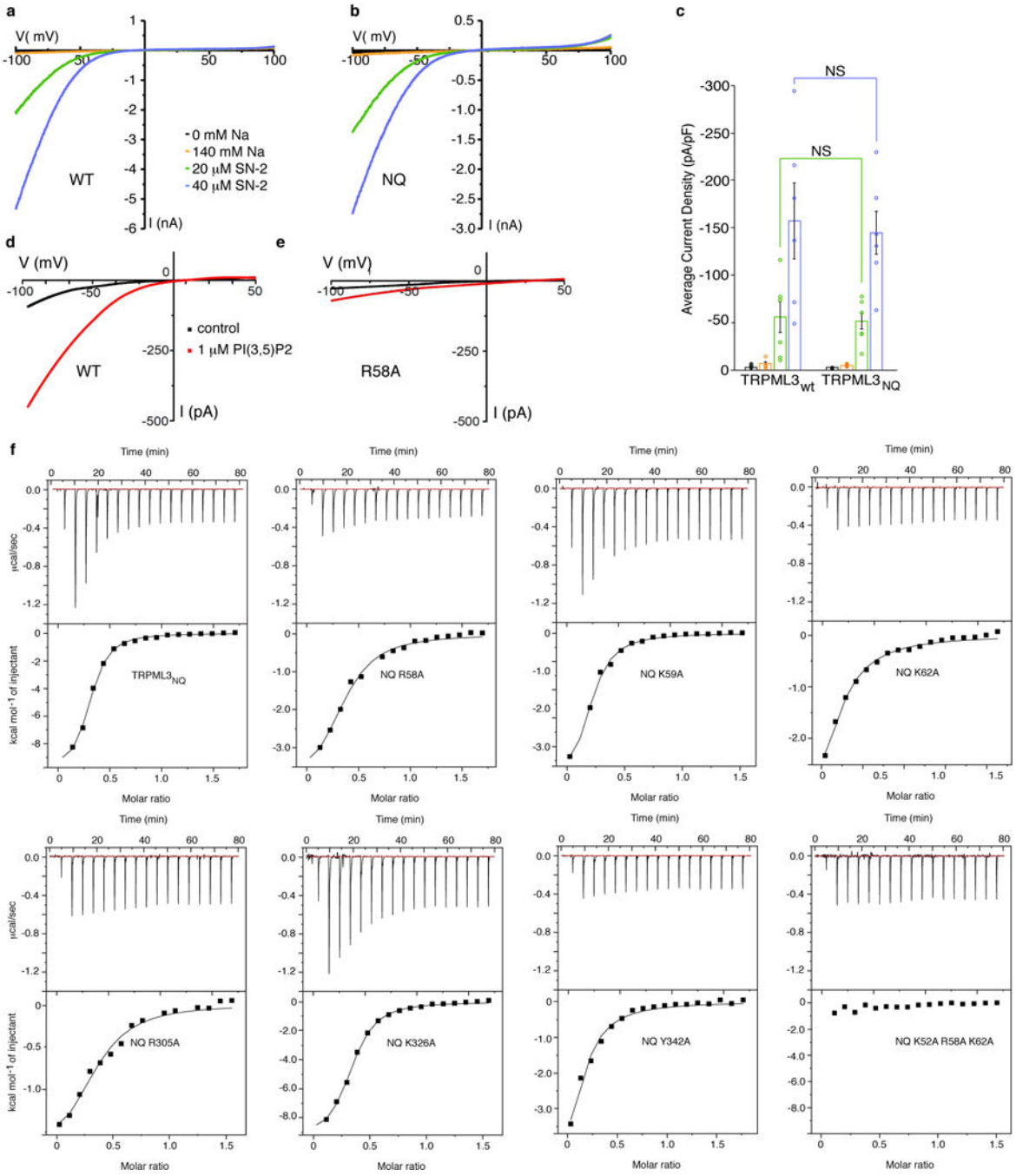

Extended Data Figure 2. Functional characterization of the TRPML3 channel and representative ITC raw data and binding isotherms for diC$_8$-PI(3,5)P$_2$ interacting with TRPML3 mutants

a, b, Representative whole-cell current traces recorded with repeated voltage ramps (from −100 to +100 mV; 400 ms; 5 s intervals between ramps) from TRPML3$_{wt}$ (**a**) and TRPML3$_{NQ}$ (**b**) transfected HEK293T cells at basal currents in 140 mM Na (orange), 0 mM Na (black), and during application of either 20 μM (green) or 80 μM (blue) of the TRPML3 agonist SN-2. **c**, Averaged inward current sizes at −100 mV normalized to cell capacitance (pA/pF) (TRPML3$_{wt}$: n = 6 biologically independent experiments; TRPML3$_{NQ}$: n = 6; open

circles represent individual experimental data points). No statistically significant differences (NS) in the current density at 20 μM ($P = 0.89$) and 80 μM ($P = 0.75$) SN-2 was determined between TRPML3 $_{wt}$ and TRPML3$_{NQ}$ (two-tailed Student's *t*-test, $P > 0.05$). Confidence intervals (95%): −2.43 (low)/1.88(high) for 0 Na^+, −6.18/4.31 for 140 Na^+, −62.69/56.84 for 20 μM SN-2 and -150.61/121.17 for 80 μM SN-2. Bar graph and error bars denote means ± s.e.m. **d, e**, Whole lysosomal current-voltage traces from TRPML3$_{wt}$ (**d**) and TRPML3$_{NQ}$ R58A (**e**), in the presence and absence of PI(3,5)P_2. Average inward currents are shown in Fig. 3f. **f**, For each TRPML3 mutant, raw ITC data and fitted binding isotherms are shown. Putative binding site mutants (Arg58Ala, Lys62Ala, Tyr342Ala, Arg305Ala and Lys52Ala/Arg58Ala/Lys62Ala) show a substantially reduced binding affinity while two negative control mutations (Lys59Ala and Lys326Ala) do not affect binding appreciably. NQ refers to N138Q mutant background. All titrations were performed in triplicate (technical replicates). Representative data are shown. Mean thermodynamic parameters for triplicate titrations are shown in the Extended Data Table 2. Mean K_d values or each triplicate are as follows: NQ 2.5 μM, NQ R58A 11.8 μM, NQ K59A 4.4 μM, NQ K62A 11.3 μM, NQ R305A 11.8 μM, NQ K326A 4.0 μM, NQ Y342A 9.4 μM, NQ K52A/R58A/K62A not determined. Due to the low heat associated with binding in many TRPML3 mutants, only the K_d values for NQ, NQ K59A, and NQ K326A are reliably measured.

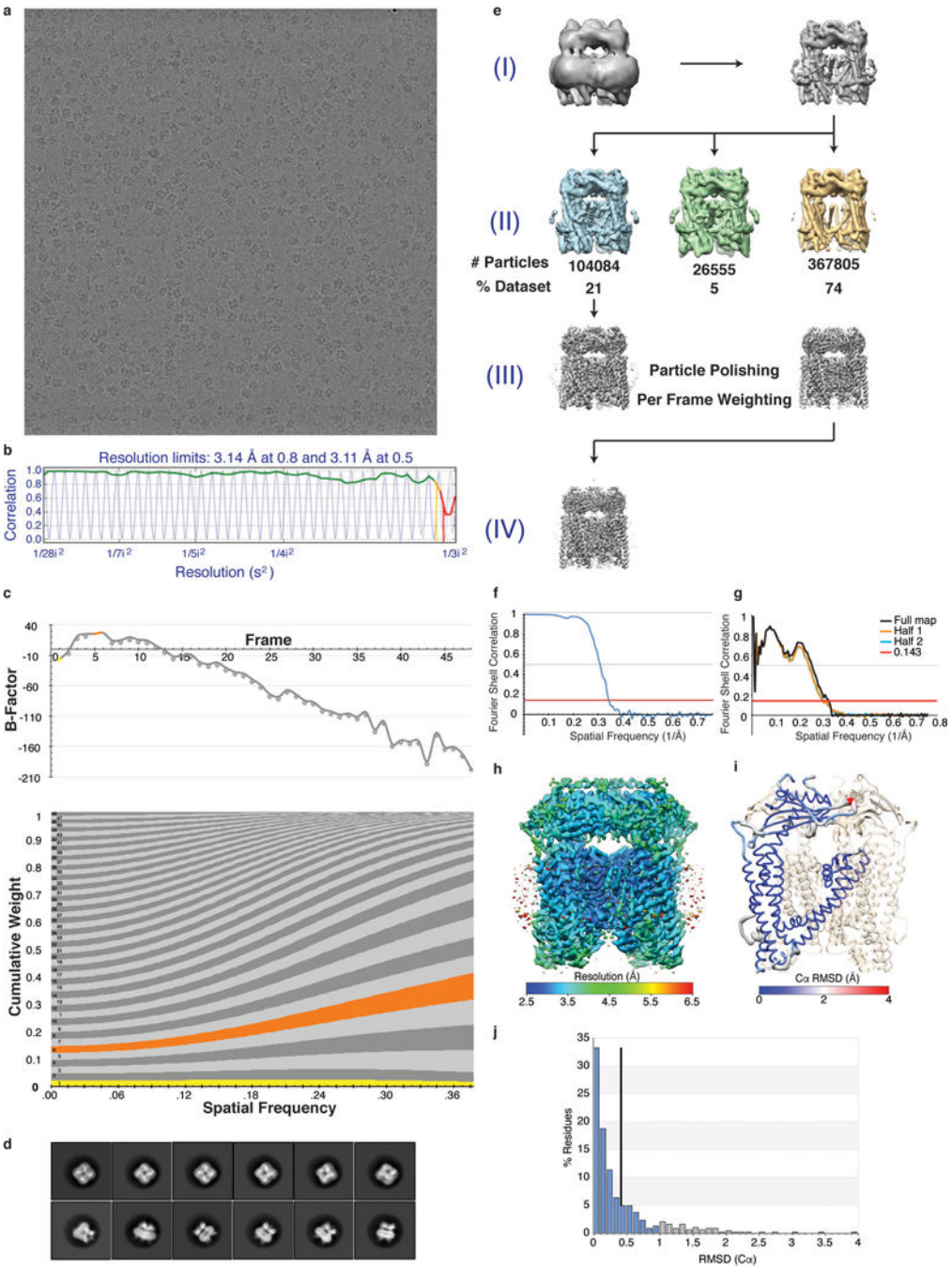

Extended Data Figure 3. Cryo-EM data collection, processing, and validation

a, b, Representative micrograph of TRPML3 in vitreous ice. We collected 2,259 movies of TRPML3. Only images exhibiting Thon rings beyond 4 Å were used for image processing, as assessed by a 1D plot (**b**). **c**, Per-frame radiation damage weighting was applied by estimating the average per-frame B Factor for all movies in the TRPML3 dataset (above). The frequency-dependent weights used to generate the final stack of summed particle images are shown below. **d**, Representative 2D class averages. **e**, Initial classification of particles into three 3D classes (II), one of which (class 1) was used for subsequent 3D

refinement. After performing the particle polishing step in RELION (III), per-particle CTF was estimated & particles were re-extracted with a box size of 512 × 512, and then refined in RELION to produce the final reconstruction (IV). **f**, Fourier Shell Correlation plot calculated from independently refined half-maps. **g**, FSC curves calculated between the atomic model and the final map (black line), and between the model and each half-map (orange and blue lines). **h**, Local resolution estimates of the final reconstructions calculated using BSOFT[45]. **i**, Worm representation with the ASU colored according to the per-residue Cα root mean square deviation (r.m.s.d.) value (Å), the rest of the molecule is colored wheat. **j**, Histogram of the per-residue Cα r.m.s.d. values calculated from the top 10 refined atomic models with the mean per-residue Cα r.m.s.d. value shown as a black vertical bar.

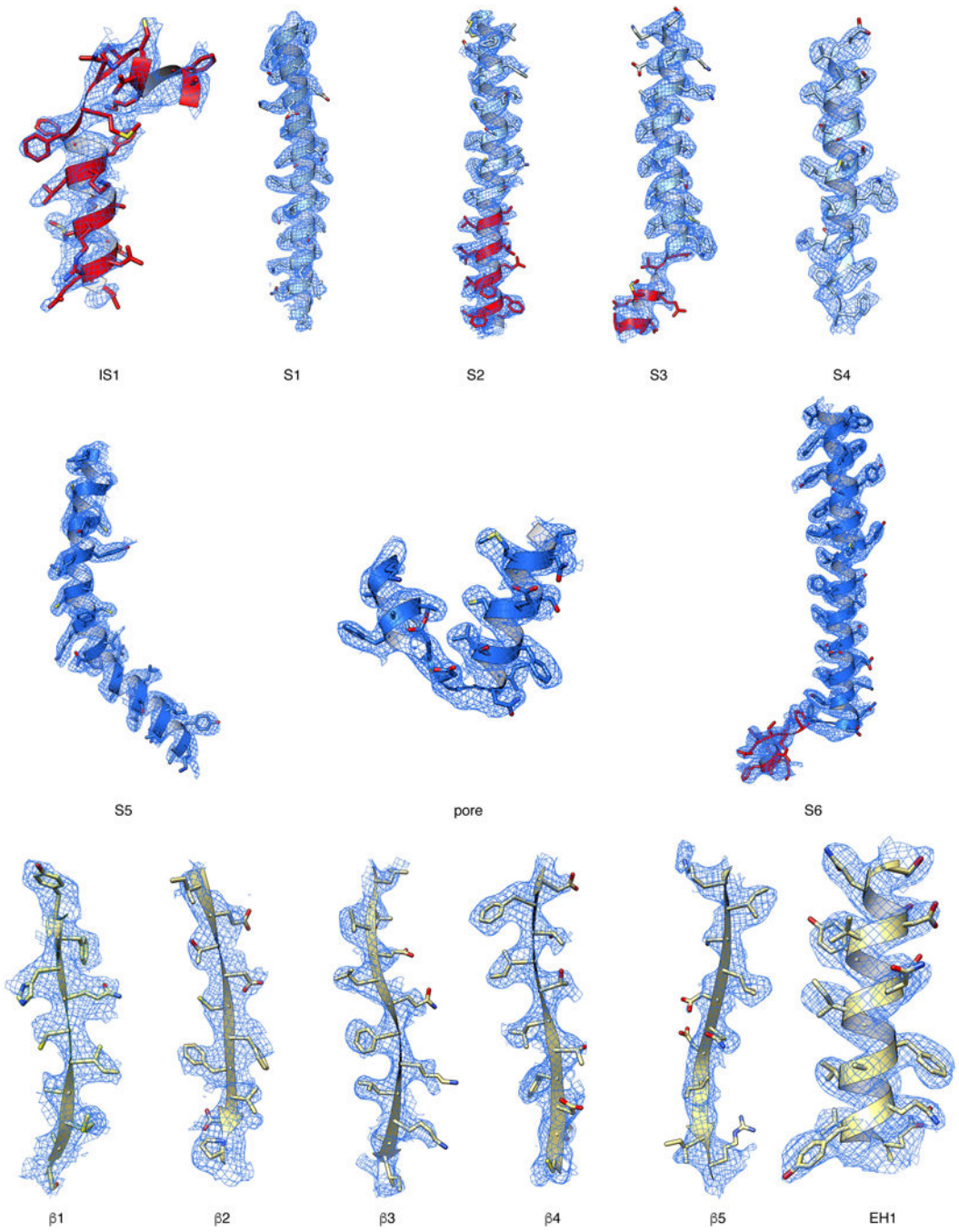

Extended Data Figure 4. Quality of cryo-EM density of key elements in the structure

The structural elements are shown in cartoon representation with side chains as sticks, colored as in Fig. 1. The cryo-EM density is shown as blue mesh.

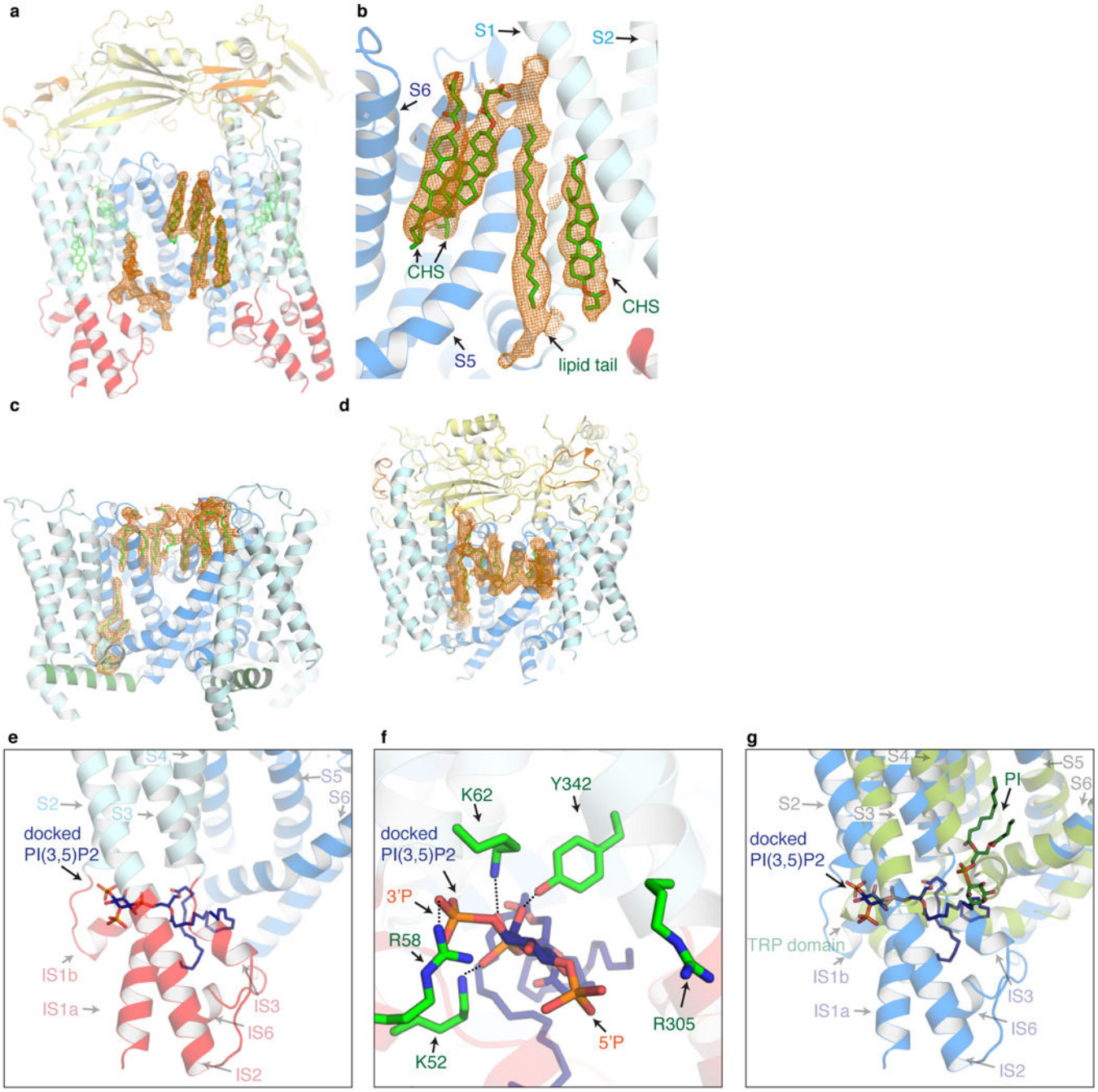

Extended Data Figure 5. Putative lipid densities in the TRPML3 map

a, Four lipid densities per protomer were resolved in the cryo-EM density and corresponding lipid molecules were built. An additional lipid density was observed near S4 of the VSLD and S5 of the pore domain, but the lipid molecule was not built due to ambiguity of the density. **b**, Two cholesteryl hemisuccinate (CHS) molecules were built in the crevice formed by S5 and S6, the third CHS molecule was fit alongside the N-terminal end of S1. In between the CHS molecules an elongated density was observed, into which a long lipid tail was built, likely from either a phospholipid or fatty acid molecule. **c, d**, Lipid densities in

analogous locations were reported for TRPV1 (**c**, PDB ID:5IRZ[14]) and PKD2 (**d**, PDB ID: 5MKE[12]). **e, f**, PI(3,5)P_2 was docked onto the TRPML3 structure, showing that the phosphoinositol headgroup docks to the basic pocket between the VSLD and MLD interacting primarily with the side-chains of Lys52, Arg58, Lys62, and Tyr342, while the acyl chains penetrate through a tunnel in the cytosolic domain to a cavity formed by S3, S4, and S6. Residues interacting with the docked PI(3,5)P_2 are shown in green (**f**). **g**, PI(3,5)P_2 (blue sticks) docked to a location in the TRPML3 structure (blue cartoon representation) distinct from the phosphoinositide (green sticks) found in the TRPV1 structure (PDB ID: 5IRZ[14], green cartoon representation) in the pocket formed by S3–S5.

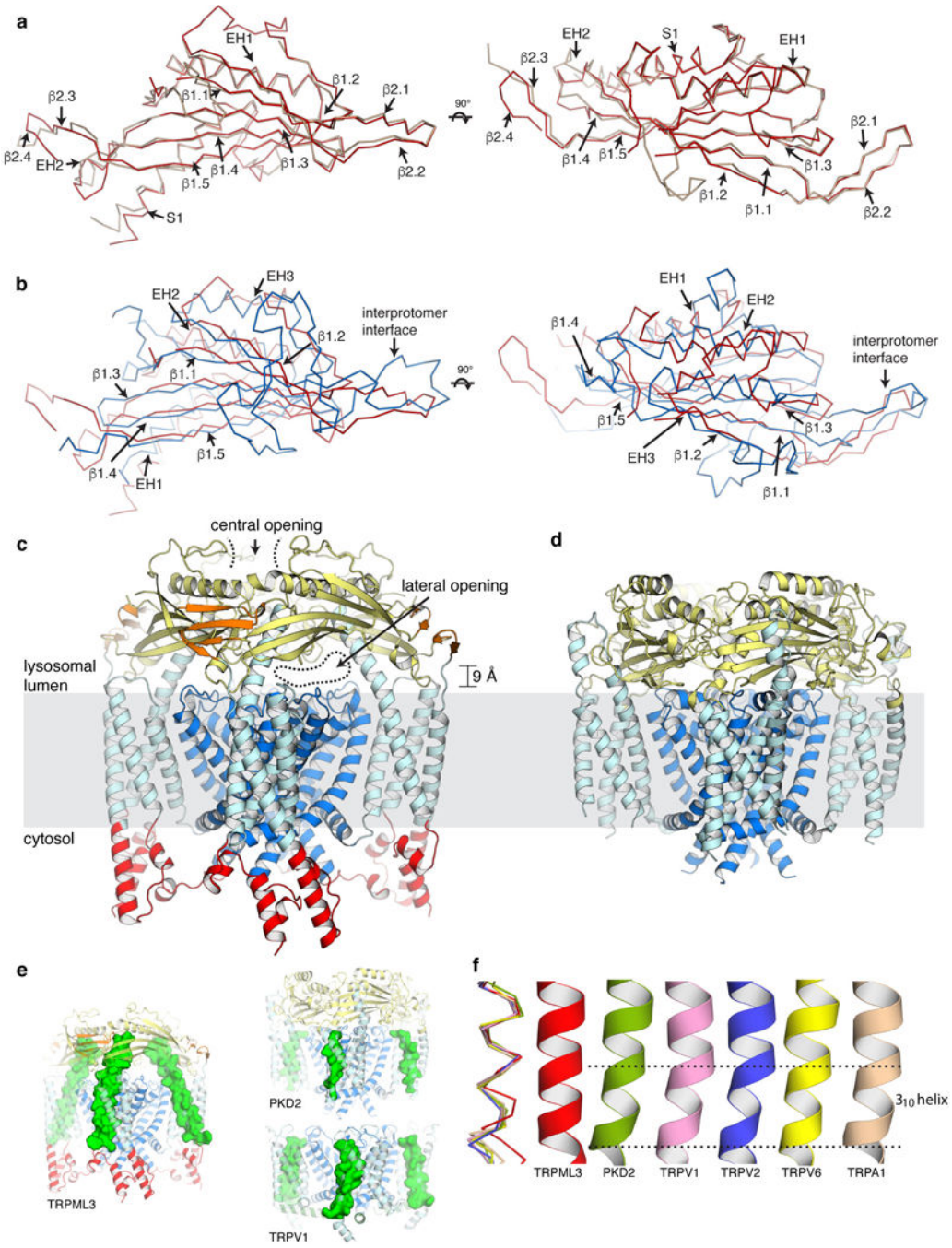

Extended Data Figure 6. Structural comparison of TRPML3 with other channels

a, The ECD from TRPML3 (red ribbon) superimposes well with the crystal structure of the ECD from TRPML1 (brown ribbon, PDBID:5TJA[15]), with a Cα r.m.s.d. of 1.8 Å. Views are shown from the membrane plane (left) and the extracytosolic side of the membrane (right). **b**, The polycystin domain from PKD2 (blue ribbon, PDBID:5T4D[13]) adopts a similar fold as the ECD from TRPML3 (red ribbon). The structural elements of PKD2 are labeled. **c**, The TRPML3 ECD lies ~9 Å away from the channel domain, which leads to limited interactions between the ECD and VSLD. **d**, The PKD2 TOP/polycystin domain lies directly on top of

the channel domain (PDBID:5T4D[13]) and forms extensive interactions with the pore. **e**, More extensive interactions are formed between S1 and the remainder of the channel in TRPML3 than in other TRP channels (buried surface areas ~3000 Å^2 and 1500–2000 Å^2, respectively). The interaction interface is shown in green. **f**, In many TRP channels a short 3_{10}-helix is present in S4. In contrast, S4 in TRPML3 is completely α-helical, suggesting a more static nature.

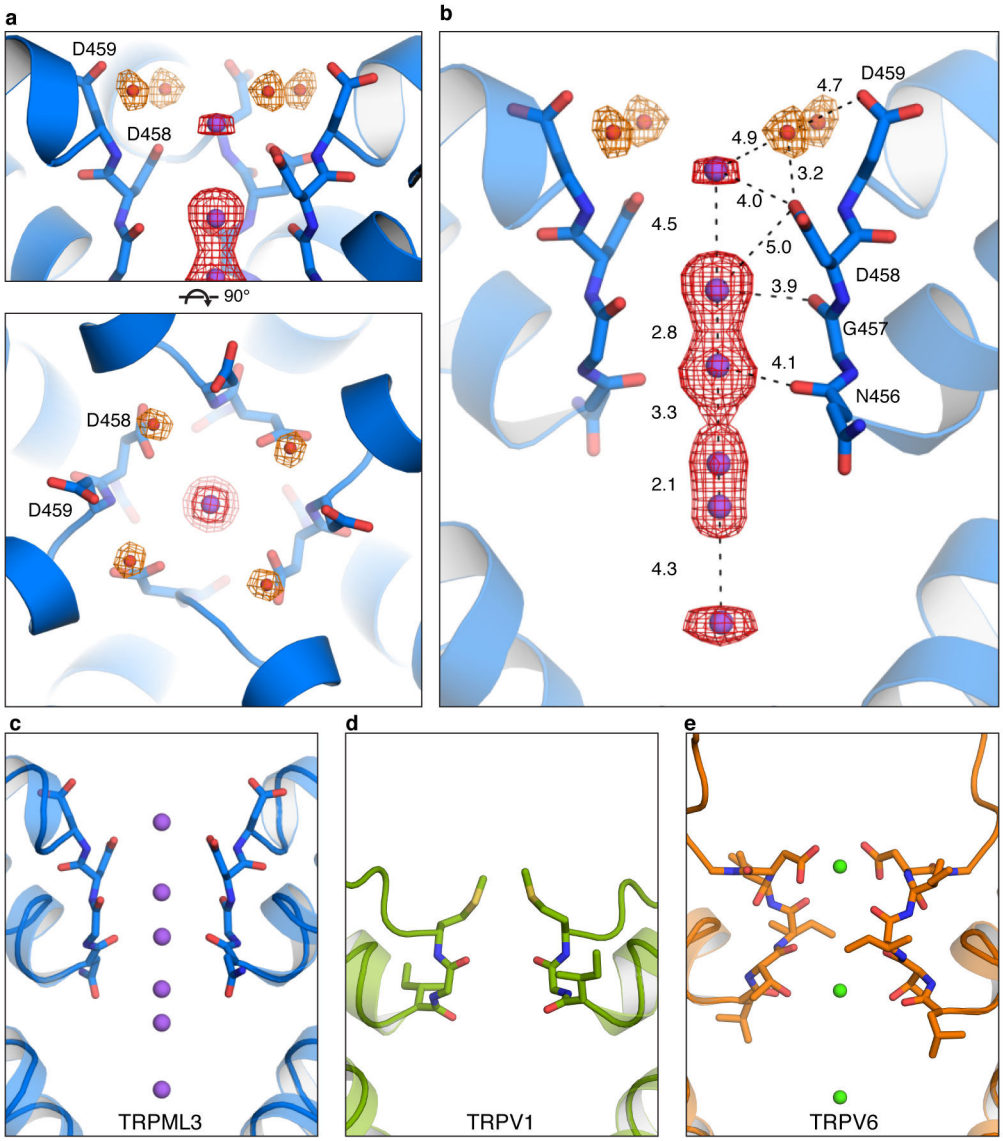

Extended Data Figure 7. Detailed view of the selectivity filter

a, Four cryo-EM density peaks observed near Asp458 and Asp459 are attributed to water molecules, based on coordination distances (~3.2 Å). TRPML3 is shown in cartoon representation with the selectivity filter residues shown as sticks. Cryo-EM density is shown in orange mesh for water molecules (red spheres) and red mesh for sodium ions (purple spheres). **b**, Interatomic distances (Å) between ions and coordinating side-chain and

backbone atoms. **c-e**, Selectivity filter comparison of TRPML3 (**c**) with TRPV1 (PDBID: 3J5P[22]) (**d**) and TRPV6 (PDBID:5IWP[21]) (**e**), with respective ions shown as spheres (purple for Na^+ and green for Ca^{2+}).

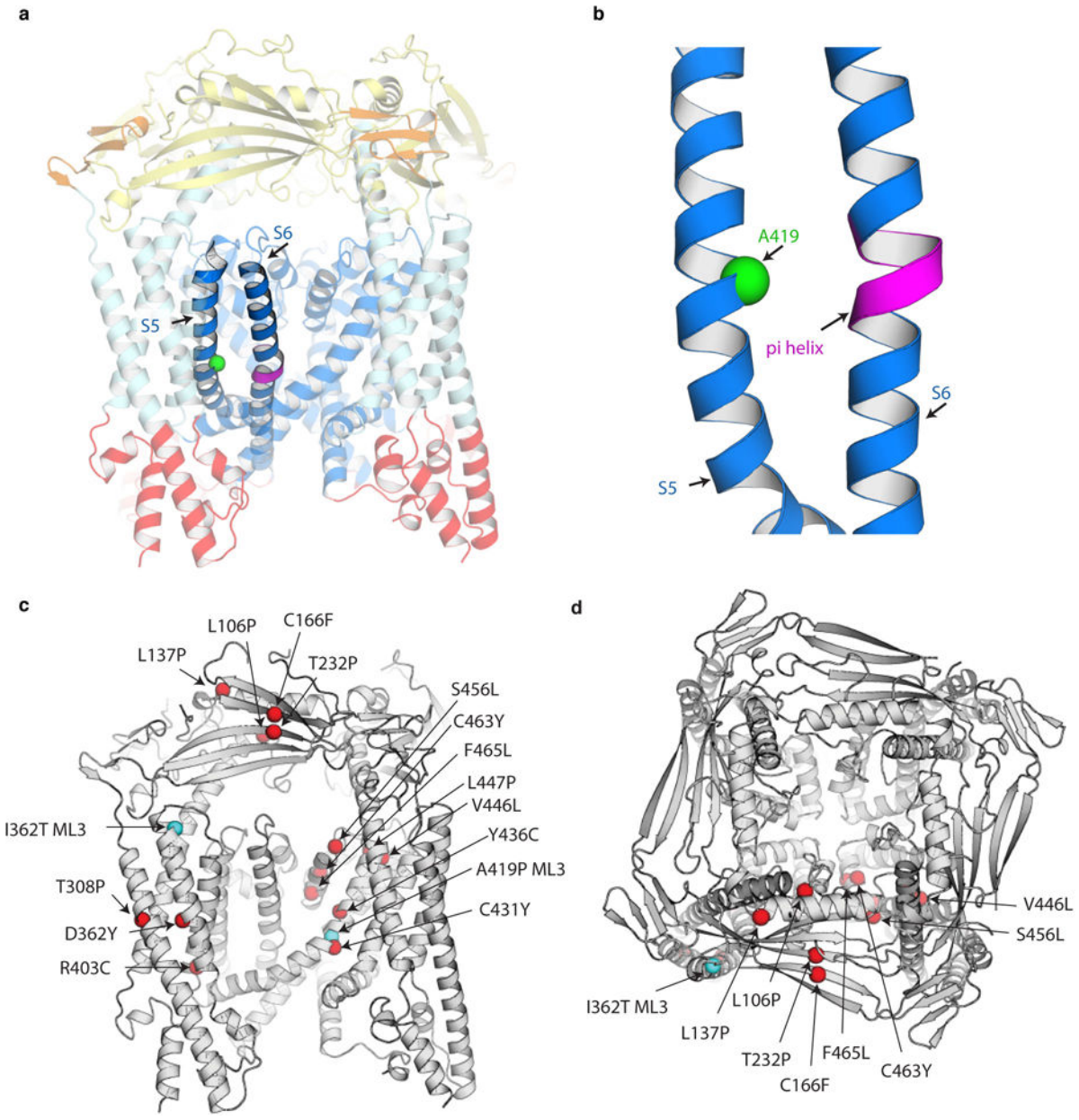

Extended Data Figure 8. The locations of the *Va* and ML-IV-causing mutations in the TRPML3 structure

a, Overview of the TRPML3 structure with the location of the Varitint-Waddler mutation Ala419Pro indicated by a green sphere and the pi helix colored magenta. TRPML3 is shown as cartoon representation, colored as in Fig. 1. **b**, Detailed view of the location of Ala419. Ala419 is positioned in the middle of S5 near the pi helix on S6, such that mutation to a proline likely disrupts normal S6 bending, locking it in an “open gate” conformation. **c, d**, Overview of the TRPML3 structure with the location of ML-IV-causing mutations indicated

by red spheres, shown from the membrane plane (**c**) and the extracytosolic side of the membrane (**d**). Unless otherwise indicated, residues are labeled using TRPML1 numbering. The locations of *Va* mutations are represented by cyan spheres. While the mutations on the ECD are associated with mild phenotypes and affect channel assembly there are many missense mutations with more severe phenotypes that are localized to the channel region. These mutations can be categorized in three groups based on their location. Mutations around pore helix 1 (group 1), mutations around S5 near A419 (group 2), and mutations within the VSLD around the PIP2-binding site (group 3). Based on our structural and functional studies, we can infer that group 1 mutations potentially disrupt ion conduction and selectivity, group 2 mutations disturb gating, and group 3 mutations affect either PIP2 binding (R403C in TRPML1) or S2 motion associated with gating (T308P and D362Y in TRPML1). Future structural and functional studies of these mutations will shed light on the molecular basis of pathogenic mutations leading to this severe neurodevelopmental disorder.

Extended Data Table 1

Data collection and refinement statistics.

Data collection	
Microscope	Titan Krios (FEI)
Voltage (keV)	300
Nominal magnification	22,500×
Electron dose (e^{-}Å^{-2})	63
Dose rate (e^{-}/pixel/sec)	9
Detector	K2 Summit (Gatan)
Pixel size (Å)	1.31 (0.655)*
Defocus range (μM)	0.8–2.8
Micrographs Used	2,259
Total extracted particles (no.)	839,127
Refined particles (no.)	498,612
Reconstruction	
Final particles (no.)	104,084
Symmetry	C4
Resolution (global)	2.9 Å
FSC 0.5 (unmasked/masked)	4.6/3.3
FSC 0.143 (unmasked/masked)	3.8/2.9
Resolution range (local)	2.7–4.7
Refinement	
Protein residues	1,940
Ligands (atoms)	1,306
Map Correlation Coefficient R.m.s. deviations	0.77
Bond lengths (Å)	0.006
Bond angles (°)	1.37
Ramachandran favored/outliers (%)	95.8/0.0
MolProbity score	1.88

Rotamer outlier (%)	0.23
Clashscore (all atoms)	4.3

* pixel size for super-resolution mode.

Extended Data Table 2

Equilibrium binding parameters showing the effect of TRPML3 mutations on diC_8-$PI(3,5)P_2$ binding.

	K_d(μM)	ΔH (kcal mol^{-1})	N (sites)
$TRPML3_{NQ}$*	2.49 ±0.11	−8.72 ± 1.28	0.3 ± 0.02
NQ R58A	11.83 ±2.86	−10.06 ±6.15	0.24 ± 0.08
NQ K59A*	4.44 ± 0.86	−12.32 ± 0.47	0.27 ± 0.05
NQ K62A	11.27 ± 1.56	−3.57 ± 1.85	0.34 ± 0.09
NQ R305A	11.78 ± 1.32	−2.25 ±0.31	0.36 ± 0.02
NQ K326A*	3.99 ± 0.26	−9.93 ± 0.35	0.30 ± 0.03
NQ Y342A	9.40 ± 1.21	−6.35 ± 1.62	0.19 ±0.05
NQ K52A/R58A/K62A	N.D.	N.D.	N.D.

Data are shown as mean ±s.e.m. of three technical replicates. Note that due to the low heat associated with binding, equilibrium parameters including Kd for the mutants are not reliably measured except for the NQ, NQ K59A, and NQ K326A mutants (*). N.D. not determined.

Acknowledgments

EM data were collected at The Scripps Research Institute (TSRI) electron microscopy facility. We thank Cheom-Gil Cheong and Seth Thomas for initial TRPML3 biochemistry, Jean-Christophe Ducom for computational support, Bill Anderson for microscope support, Saikat Chowdhury for aiding in preliminary EM analyses, Alvin Kuk for help with the docking study, and Richard Brennan and Maria Schumacher for providing access to ITC equipment. This work was supported by the National Institutes of Health (R35NS097241 to S.-Y. L., DP2EB020402 to G.C.L., R01NS055293 and R01NS074257 to D. R.). G.C.L is supported as a Searle Scholar and a Pew Scholar. M.A.H was supported by a Helen Hay Whitney Foundation postdoctoral fellowship. Computational analyses of EM data were performed using shared instrumentation funded by NIH S10OD021634.

References

1. Ramsey IS, Delling M, Clapham DE. An introduction to TRP channels. Annu Rev Physiol. 2006; 68:619–647. DOI: 10.1146/annurev.physiol.68.040204.100431 [PubMed: 16460286]
2. Julius D. TRP channels and pain. Annu Rev Cell Dev Biol. 2013; 29:355–384. DOI: 10.1146/annurev-cellbio-101011-155833 [PubMed: 24099085]
3. Xu H, Ren D. Lysosomal physiology. Annu Rev Physiol. 2015; 77:57–80. DOI: 10.1146/annurev-physiol-021014-071649 [PubMed: 25668017]
4. Bargal R, et al. Identification of the gene causing mucolipidosis type IV. Nature genetics. 2000; 26:118–123. DOI: 10.1038/79095 [PubMed: 10973263]
5. Di Palma F, et al. Mutations in Mcoln3 associated with deafness and pigmentation defects in varitint-waddler (Va) mice. Proceedings of the National Academy of Sciences of the United States of America. 2002; 99:14994–14999. DOI: 10.1073/pnas.222425399 [PubMed: 12403827]
6. Xu H, Delling M, Li L, Dong X, Clapham DE. Activating mutation in a mucolipin transient receptor potential channel leads to melanocyte loss in varitint-waddler mice. Proceedings of the National Academy of Sciences of the United States of America. 2007; 104:18321–18326. DOI: 10.1073/pnas.0709096104 [PubMed: 17989217]
7. Dong XP, et al. PI(3,5)P(2) controls membrane trafficking by direct activation of mucolipin Ca(2+) release channels in the endolysosome. Nature communications. 2010; 1:38.

8. Zhang X, Li X, Xu H. Phosphoinositide isoforms determine compartment-specific ion channel activity. Proceedings of the National Academy of Sciences of the United States of America. 2012; 109:11384–11389. DOI: 10.1073/pnas.1202194109 [PubMed: 22733759]
9. Kim HJ, et al. A novel mode of TRPML3 regulation by extracytosolic pH absent in the varitint-waddler phenotype. The EMBO journal. 2008; 27:1197–1205. DOI: 10.1038/emboj.2008.56 [PubMed: 18369318]
10. Kim HJ, et al. Gain-of-function mutation in TRPML3 causes the mouse Varitint-Waddler phenotype. The Journal of biological chemistry. 2007; 282:36138–36142. DOI: 10.1074/jbc.C700190200 [PubMed: 17962195]
11. Grimm C, et al. Small molecule activators of TRPML3. Chem Biol. 2010; 17:135–148. DOI: 10.1016/j.chembiol.2009.12.016 [PubMed: 20189104]
12. Wilkes M, et al. Molecular insights into lipid-assisted Ca2+ regulation of the TRP channel Polycystin-2. Nature structural & molecular biology. 2017; 24:123–130. DOI: 10.1038/nsmb.3357
13. Shen PS, et al. The Structure of the Polycystic Kidney Disease Channel PKD2 in Lipid Nanodiscs. Cell. 2016; 167:763–773 e711. DOI: 10.1016/j.cell.2016.09.048 [PubMed: 27768895]
14. Gao Y, Cao E, Julius D, Cheng Y. TRPV1 structures in nanodiscs reveal mechanisms of ligand and lipid action. Nature. 2016; 534:347–351. DOI: 10.1038/nature17964 [PubMed: 27281200]
15. Li M, et al. Structural basis of dual Ca2+/pH regulation of the endolysosomal TRPML1 channel. Nature structural & molecular biology. 2017
16. Grieben M, et al. Structure of the polycystic kidney disease TRP channel Polycystin-2 (PC2). Nature structural & molecular biology. 2017; 24:114–122. DOI: 10.1038/nsmb.3343
17. Paulsen CE, Armache JP, Gao Y, Cheng Y, Julius D. Structure of the TRPA1 ion channel suggests regulatory mechanisms. Nature. 2015; 520:511–517. DOI: 10.1038/nature14367 [PubMed: 25855297]
18. Cao E, Liao M, Cheng Y, Julius D. TRPV1 structures in distinct conformations reveal activation mechanisms. Nature. 2013; 504:113–118. DOI: 10.1038/nature12823 [PubMed: 24305161]
19. Zubcevic L, et al. Cryo-electron microscopy structure of the TRPV2 ion channel. Nature structural & molecular biology. 2016
20. Gregorio-Teruel L, et al. The Integrity of the TRP Domain Is Pivotal for Correct TRPV1 Channel Gating. Biophys J. 2015; 109:529–541. DOI: 10.1016/j.bpj.2015.06.039 [PubMed: 26244735]
21. Saotome K, Singh AK, Yelshanskaya MV, Sobolevsky AI. Crystal structure of the epithelial calcium channel TRPV6. Nature. 2016; 534:506–511. DOI: 10.1038/nature17975 [PubMed: 27296226]
22. Liao M, Cao E, Julius D, Cheng Y. Structure of the TRPV1 ion channel determined by electron cryo-microscopy. Nature. 2013; 504:107–112. DOI: 10.1038/nature12822 [PubMed: 24305160]
23. Tang L, et al. Structural basis for Ca2+ selectivity of a voltage-gated calcium channel. Nature. 2014; 505:56–61. DOI: 10.1038/nature12775 [PubMed: 24270805]
24. Naylor CE, et al. Molecular basis of ion permeability in a voltage-gated sodium channel. The EMBO journal. 2016; 35:820–830. DOI: 10.15252/embj.201593285 [PubMed: 26873592]
25. Kim HJ, Yamaguchi S, Li Q, So I, Muallem S. Properties of the TRPML3 channel pore and its stable expansion by the Varitint-Waddler-causing mutation. The Journal of biological chemistry. 2010; 285:16513–16520. DOI: 10.1074/jbc.M109.078204 [PubMed: 20378547]
26. Venkatachalam K, Wong CO, Zhu MX. The role of TRPMLs in endolysosomal trafficking and function. Cell Calcium. 2015; 58:48–56. DOI: 10.1016/j.ceca.2014.10.008 [PubMed: 25465891]
27. AlBakheet A, et al. A novel mutation in a large family causes a unique phenotype of Mucolipidosis IV. Gene. 2013; 526:464–466. DOI: 10.1016/j.gene.2013.04.076 [PubMed: 23685283]
28. Tuysuz B, Goldin E, Metin B, Korkmaz B, Yalcinkaya C. Mucolipidosis type IV in a Turkish boy associated with a novel MCOLN1 mutation. Brain Dev. 2009; 31:702–705. DOI: 10.1016/j.braindev.2008.10.001 [PubMed: 19006653]
29. Bach G. Mucolipidosis type IV. Mol Genet Metab. 2001; 73:197–203. DOI: 10.1006/mgme.2001.3195 [PubMed: 11461186]
30. Suloway C, et al. Automated molecular microscopy: the new Leginon system. J Struct Biol. 2005; 151:41–60. DOI: 10.1016/j.jsb.2005.03.010 [PubMed: 15890530]

31. Lander GC, et al. Appion: an integrated, database-driven pipeline to facilitate EM image processing. J Struct Biol. 2009; 166:95–102. [PubMed: 19263523]
32. Voss NR, Yoshioka CK, Radermacher M, Potter CS, Carragher B. DoG Picker and TiltPicker: software tools to facilitate particle selection in single particle electron microscopy. J Struct Biol. 2009; 166:205–213. [PubMed: 19374019]
33. Rohou A, Grigorieff N. CTFFIND4: Fast and accurate defocus estimation from electron micrographs. J Struct Biol. 2015; 192:216–221. DOI: 10.1016/j.jsb.2015.08.008 [PubMed: 26278980]
34. Ludtke SJ, Baldwin PR, Chiu W. EMAN: semiautomated software for high-resolution single-particle reconstructions. J Struct Biol. 1999; 128:82–97. DOI: 10.1006/jsbi.1999.4174 [PubMed: 10600563]
35. Ogura T, Iwasaki K, Sato C. Topology representing network enables highly accurate classification of protein images taken by cryo electron-microscope without masking. J Struct Biol. 2003; 143:185–200. [PubMed: 14572474]
36. Scheres SH. RELION: implementation of a Bayesian approach to cryo-EM structure determination. Journal of structural biology. 2012; 180:519–530. DOI: 10.1016/j.jsb.2012.09.006 [PubMed: 23000701]
37. Li X, et al. Electron counting and beam-induced motion correction enable near-atomic-resolution single-particle cryo-EM. Nat Methods. 2013; 10:584–590. DOI: 10.1038/nmeth.2472 [PubMed: 23644547]
38. Roseman AM. FindEM–a fast, efficient program for automatic selection of particles from electron micrographs. J Struct Biol. 2004; 145:91–99. [PubMed: 15065677]
39. Scheres SH. Beam-induced motion correction for sub-megadalton cryo-EM particles. Elife. 2014; 3:e03665. [PubMed: 25122622]
40. Scheres SH, Chen S. Prevention of overfitting in cryo-EM structure determination. Nat Methods. 2012; 9:853–854. DOI: 10.1038/nmeth.2115 [PubMed: 22842542]
41. Rosenthal PB, Henderson R. Optimal determination of particle orientation, absolute hand, and contrast loss in single-particle electron cryomicroscopy. J Mol Biol. 2003; 333:721–745. [PubMed: 14568533]
42. Zheng SQ, et al. MotionCor2: anisotropic correction of beam-induced motion for improved cryo-electron microscopy. Nat Methods. 2017; 14:331–332. DOI: 10.1038/nmeth.4193 [PubMed: 28250466]
43. Kimanius D, Forsberg BO, Scheres SH, Lindahl E. Accelerated cryo-EM structure determination with parallelisation using GPUs in RELION-2. Elife. 2016; 5
44. Chen S, et al. High-resolution noise substitution to measure overfitting and validate resolution in 3D structure determination by single particle electron cryomicroscopy. Ultramicroscopy. 2013; 135:24–35. DOI: 10.1016/j.ultramic.2013.06.004 [PubMed: 23872039]
45. Heymann JB, Belnap DM. Bsoft: image processing and molecular modeling for electron microscopy. J Struct Biol. 2007; 157:3–18. DOI: 10.1016/j.jsb.2006.06.006 [PubMed: 17011211]
46. Goddard TD, Huang CC, Ferrin TE. Visualizing density maps with UCSF Chimera. J Struct Biol. 2007; 157:281–287. DOI: 10.1016/j.jsb.2006.06.010 [PubMed: 16963278]
47. Emsley P, Cowtan K. Coot: model-building tools for molecular graphics. Acta crystallographica Section D, Biological crystallography. 2004; 60:2126–2132. doi:S0907444904019158. [PubMed: 15572765]
48. Adams PD, et al. PHENIX: a comprehensive Python-based system for macromolecular structure solution. Acta crystallographica Section D, Biological crystallography. 2010; 66:213–221. DOI: 10.1107/S0907444909052925 [PubMed: 20124702]
49. Smart OS, Neduvelil JG, Wang X, Wallace BA, Sansom MS. HOLE: a program for the analysis of the pore dimensions of ion channel structural models. Journal of molecular graphics. 1996; 14:354–360. 376. [PubMed: 9195488]
50. Goehring A, et al. Screening and large-scale expression of membrane proteins in mammalian cells for structural studies. Nat Protoc. 2014; 9:2574–2585. DOI: 10.1038/nprot.2014.173 [PubMed: 25299155]

51. Cang C, et al. mTOR regulates lysosomal ATP-sensitive two-pore Na(+) channels to adapt to metabolic state. Cell. 2013; 152:778–790. DOI: 10.1016/j.cell.2013.01.023 [PubMed: 23394946]

52. Trott O, Olson AJ. AutoDock Vina: improving the speed and accuracy of docking with a new scoring function, efficient optimization, and multithreading. Journal of computational chemistry. 2010; 31:455–461. DOI: 10.1002/jcc.21334 [PubMed: 19499576]

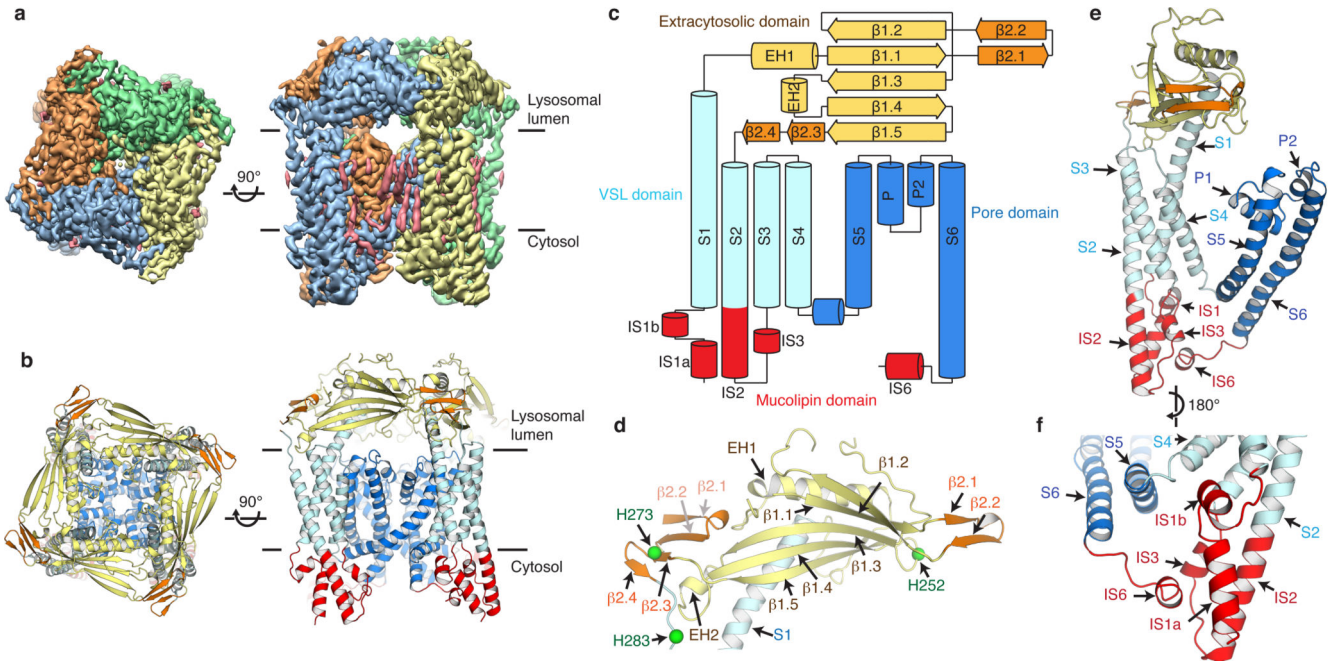

Figure 1. Overall topology of the TRPML3 channel

a, b, Cryo-EM reconstruction **(a)** and model **(b)** of TRPML3 viewed from the extracytosolic side (left) and from the membrane plane (right). **c**, Topology diagram delineating the protein domains and their secondary structures. **d–f**, Detailed view of the ECD (histidines implicated in pH-sensing indicated by green spheres) (**d**), a TRPML3 protomer (**e**), and the mucolipin domain (**f**).

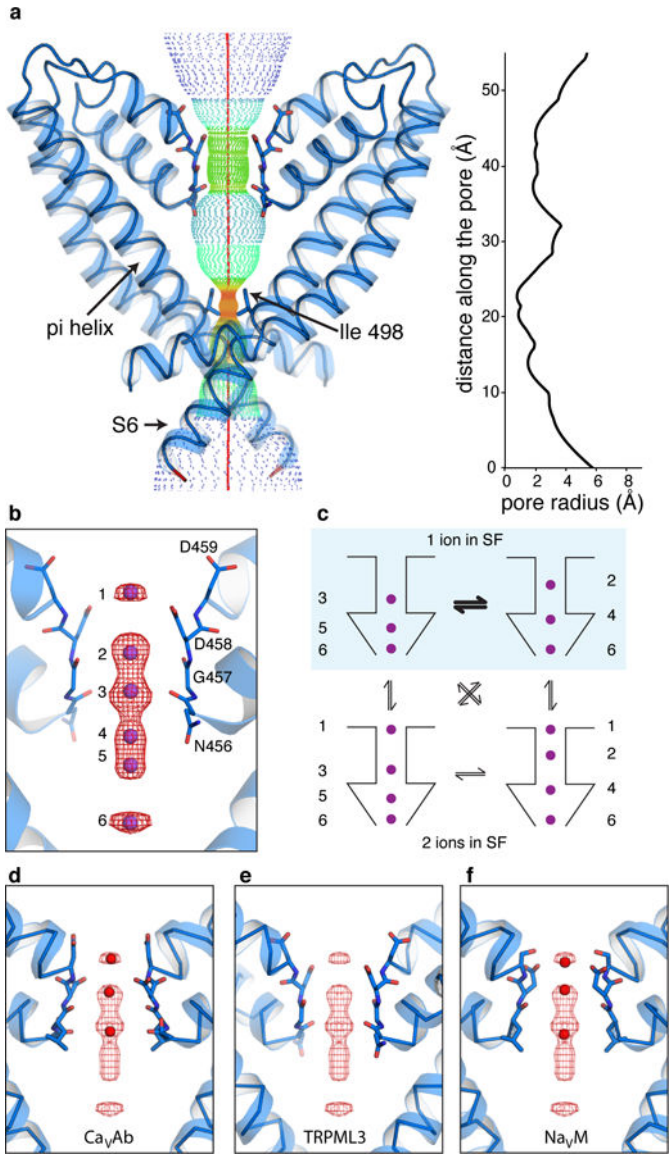

Figure 2. Pore and selectivity filter structure

a, Radius along the permeation pathway. **b**, Six sodium ions (purple) were built into cryo-EM density peaks (red mesh). **c**, Proposed main sodium-occupied states, with most populated states highlighted in blue. **d-f**, Selectivity filter comparison with Ca_VAb (PDBID: 5KLB[23]) (**d**) and Na_VM (PDBID:5BZB[24]) (**f**), with the TRPML3 ion densities shown as red mesh, with atomic coordinates of respective ions shown as red spheres.

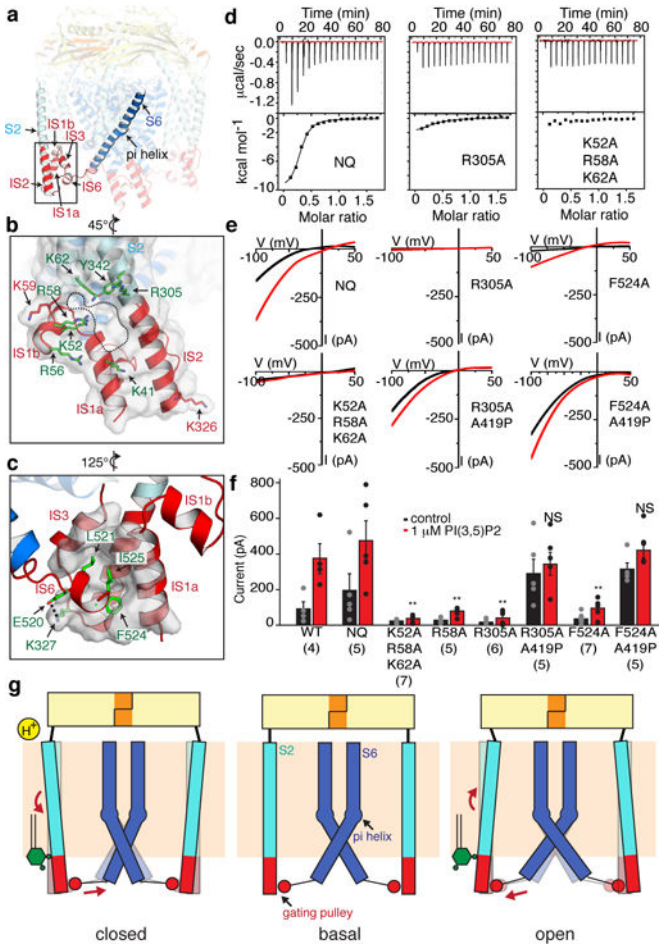

Figure 3. Putative PIP_2 binding site and proposed gating pulley mechanism

a, b, The putative PIP_2 binding site is located within a pocket of the mucolipin domain (**a**) where many basic residues (green) localize (**b**). **c**, IS6 fits tightly into a hydrophobic pocket formed by IS1a, IS3 and IS2, key residues shown in green. **d**, Mutations of the binding site reduce diC_8-$PI(3,5)P_2$ binding substantially. Representative ITC data of three technical replicates, see Extended Data Fig. 8 for details. **e, f**, Whole lysosomal current-voltage relationships (**e**) and current amplitudes at −100 mV (**f**), in the presence and absence of $PI(3,5)P_2$. Data is presented as mean ± s.e.m., with each individual data point overlaying the bar. Number of lysosomes recorded (technical replicates) are in parentheses. Statistical tests were performed to compare the sizes of $PI(3,5)P_2$ –activated currents in the mutants with those in $TRPML3_{NQ}$. **, $P < 0.01$ by a two-tailed Student's *t*-test. P-values: 0.0007 for Lys52Ala/Arg58Ala/Lys62Ala, 0.007 for Arg58Ala, 0.002 for Arg305Ala, 0.002 for Phe524Ala. Confidence intervals (95%): 232.8 (low)/642.7(high) for Lys52Ala/Arg58Ala/Lys62Ala, 139.4/650.5 for Arg58Ala, 202.3/660.4 for Arg305Ala, 168.1/585.7 for Phe524Ala. **g**, A model by which the MLD (red) propagates signals from the ECD or PIP_2 (green) binding to the S6 gate. Protons (yellow) and $PI(4,5)P_2$ induce a conformational change in S2 that relays through the gating pulley (MLD) to bending of S6 at the pi-helix to

close the pore while $PI(3,5)P_2$ binding induces a distinct change in S2 that leads to pore opening.